EAGLE Internal Note
INDET-NO-009
April 30, 1992

A Radiation Hard Detector for Tracking and Secondary Vertex Finding for the EAGLE Detector at the CERN LHC.

C. Arrighi, J.-C. Clemens, M. Cohen-Solal, M. Commerçon, P. Delpierre, A. Falou, M-C. Habrard, G. Hallewell, L. Lopez, A. Mekkaoui, Th. Mouthuy, D. Sauvage

Centre de Physique des Particules de Marseille,
163, Avenue de Luminy, Case 907,
13288 Marseille Cedex 09,
France.

Abstract.

We propose to develop a radiation-hard inner tracking and vertex detector for use at the CERN Large Hadron Collider (LHC). The detector combines pixels with silicon microstrip detectors to solve combinatorics associated with ghost hits, and is intended to contribute to accurate momentum measurement in the central region for pseudo-rapidity in the range $-2.0 \leq \eta \leq 2.0$, and to allow efficient **b** tagging through secondary vertex localisation. The detector is intended to operate efficiently at the high design luminosity of LHC, and to have sufficient acceptance to accomodate an axial variation of 8 cm (1σ) in the LHC beam collision point. We consider the special demands this physics coverage at the high LHC luminosity would make on the detector geometry, granularity and radiation hardness, and go on to discuss some details of the construction of the detector and our proposed research and development program.

Contents

(1) Introduction.

We propose to develop a radiation-hard vertex and inner tracking detector for use at the CERN Large Hadron Collider (LHC). The detector is intended to provide accurate momentum measurement and secondary vertex localisation in the central region (pseudo-rapidity up to 2.0), from a combination of silicon microstrip detectors and pixel detectors, located to maximum advantage. The considerable physics interest currently directed in this rapidity range is summarised in ref (1)

The principal areas of physics opportunity in the central rapidity region ($-2.0 \leq \eta \leq 2.0$) are summarised in ref (1). Refs (2-4) further discuss the location of the inner tracking and vertex detector and the secondary vertex position resolution and $\Delta P/P$ resolution necessary to study some of the physics of interest.

Using the JETSET 7.3 {ref (5)} and PYTHIA 5.6 {ref (6)} programs, we have made a series of Monte Carlo simulations of the performance of an inner tracking and vertex detector covering 2.0 units of rapidity.

We have compared the performance of a silicon microstrip and pixel detector in rapidity this region, subject to the best available estimates of charged track multiplicity at the nominal LHC luminosity of $2.10^{34}\,cm^{-2}\,sec^{-1}$. In particular, we find that the efficiency of an innermost pixel detector array for separation of multiple tracks from overlaid events is superior to that of a silicon strip detector. We also find that the multi-hit performance of an orthogonal, double sided silicon strip detector is greatly reduced by the presence of ghost hits in the high density environment of LHC collisions.

We have also tried to evolve a detector geometry with simplicity of mechanical support and relative ease of alignment and survey. We go on to discuss the construction of the detector and our proposed longer-term research and development program.

(2) The Detector Design Criteria

(2.1) Detector Layout

Fig (1) shows the proposed detector geometry. In the central region, cylindrical arrays of silicon microstrip detectors at nominal radii of 20 and 32 cm surround inner arrays of silicon or

gallium arsenide pixel detectors at a nominal radius of 11.5 cm. All cylindrical arrays have an axial length 100 cm. At the nominal radius of 32 cm from the beam axis (where space points are particularly important for tracking, we propose two nested cylindrical arrays of silicon microstrip detectors for redundancy. The central cylindrical array (at 20 cm radius) can be a single layer of silicon microstrips. The innermost layer is again very important for vertex determination, and we propose a double layer of silicon or gallium arsenide pixel detectors at 11.5 cm. At this radius it will be subject to a high radiation dose, as discussed in §5.

At each end of the cylindrical tracker, two truncated conical surfaces are located, which allow measurement for rapidities in the range 1.2 to 2.0. The outermost conical surface is a double layer of silicon microstrips, while innermost is a layer of silicon or gallium arsenide pixel detectors. We see now that the proposed geometry of fig (1) represents a compromise between detector surface area and radiation damage. Nowhere do the cylinders (truncated conic surfaces) come closer to the beam axis than 11.5 (15.5) cm.

All the detector array surfaces will be tesselated from tiles or "plaquettes" of pixel or silicon microstrip detectors. In this physics simulation, we have assumed a plaquette dimension 50 X 32 mm^2; fairly typical of the silicon microstrip detectors presently in operation.

(2.2) Tracking Efficiency.

The tracking efficiency of the silicon detector is determined from the number of hits found in each layer of the detector.

In an analysis similar to that made by Gadomski {Ref (7)} for a different detector geometry, we have estimated the mean number of charged tracks passing through a detector covering 2.0 units of rapidity at LHC luminosities of 10^{33}, 10^{34} and 2.10^{34} cm^{-2} sec^{-1} to be respectively 62, 293 and 604. The mean number of tracks per high P_T event is 38 (P_T cut at 10 GeV); increasing the P_T cut to 1 TeV increases the mean number of charged tracks to 140. Similarly, the number of tracks per minimum bias event is found to be 12.

In the case of a detector constructed solely from silicon microstrip planes, two effects will degrade the tracking efficiency:

(i) in a high multiplicity environment, two or more unresolvable tracks might cross the same strip. This effect is small when the strip width is narrow. For example, a particular strip of width 50 mm and length 5 cm located 11.5 cm from the interaction point is hit more than once in only 0.1% of events, even at a luminosity up to 2 10^{34} cm^{-2} sec^{-1}.

(ii) when crossed strips are used to provide 2 coordinates readout in a high multiplicity environment, ambiguities arise in the assignment of strips to a given track due to ghost hits. A small stereo angle may be employed to help reduce the number of ghosts in a particular plaquette by moving them out of the plaquette, but this can only be done with loss of spatial resolution in one of the co-ordinates. Eventually this will lead to a failure in finding the secondary vertex.

At a luminosity of 2 10^{34} cm^{-2} sec^{-1}, when hit, a 50 x 32 mm^2 plaquette located at a radius of 11.5 cm from the beam axis will be hit by on average 2 tracks per event.

Number of Hits per plaquette	Fraction (%)	Number of Ghost Hits	Number of Ambiguous Solutions to Choose Between
1	44.3	0	1
2	29.2	2	2
3	14.8	6	6
4	6.7	12	24
5	3.0	20	120
6	1.3	30	720
7	0.42	42	5040
8	0.13	56	40320
9	0.056	72	362880
10	0.012	90	3628800
11	0.006	110	39916800

Table (1) Distribution of hits, ghosts and pattern recognition ambiguities in a 50 x 32 mm^2 microstrip plaquette located 11.5 cm from the beam axis: L = 2 10^{34} cm^{-2} sec^{-1}

Multiple track hits in microstrip plaquettes located close to the beam axis would cause an enormous pattern recognition ambiguity problem. In each plaquette, the number of ghost hits added to the **n** real track impacts is given by **n(n-1),** but the number of solutions from which to choose the real track impact combination is **n!.** Out

of these **n!** solutions, only one is correct. The distribution of hits per plaquette is shown in table (1).

Table (2) shows the track multiplicity through a 50 x 32 mm^2 plaquette as a function of both luminosity and distance from the interaction point. The mean numbers of ghost hits and ambiguities from which to find the real track impacts are also shown for each track multiplicity distribution.

Number of Hits per plaquette	11.5 cm from I.P. Luminosity ($cm^{-2}s^{-1}$)			20 cm from I.P. Luminosity ($cm^{-2}s^{-1}$)		
	10^{33}	10^{34}	2.10^{34}	10^{33}	10^{34}	2.10^{34}
1	89.1%	65.0%	44.3%	96.0%	84.2%	71.6%
2	9.62%	25.0%	29.2%	3.84%	13.5%	21.6%
3	1.14%	7.32%	19.8%	0.17%	2.03%	5.45%
4	0.033%	1.80%	6.70%	-	0.26%	1.16%
5	0.007%	0.668%	3.02%	-	0.020%	0.148%
6	-	0.130%	1.34%	-	-	0.045%
7	-	0.046%	0.422%	-	-	-
8	-	0.018%	0.130%	-	-	-
9	-	0.009%	0.056%	-	-	-
10	-	-	0.012%	-	-	-
11	-	-	0.006%	-	-	-
Mean Number of Ghosts	0.278	1.36	3.59	0.0087	0.427	0.941
Mean Number of Ambiguous Choices	1.24	46.0	3124	1.047	1.320	2.26

Table (2) Hit Multiplicity Distributions, mean numbers of ghost hits and pattern recognition ambiguities in a 50 x 32 mm^2 plaquette located 11.5 & 20 cm from the beam axis for L = 10^{33}, 10^{34} and 2 10^{34} cm^{-2} s^{-1}

At a distance of 20 cm, the pattern recognition ambiguity problem is dramatically reduced, with an average of only 0.9 ghost hits and 2.26 ambiguous solutions to choose between at **L = 2 10^{34}.**

We have simulated gluon and quark jets at 1 TeV with PYTHIA and JETSET, and expect gluon (quark) jets to contain about 7 (5) tracks

within $\pm 1\sigma$ and about 12 (8) within $\pm 3\sigma$, with an angular width of 11.8 and 5.6 mrad respectively ($\pm 1\sigma$). For comparison at lower energy, at 24.5 GeV {ref (9)}, quark jets contain an average of 12.5 particles, of which 7.2 are charged, while for gluon jets the corresponding numbers are 12.9 and 7.4 respectively.

The opening angles between the particles in the jet are an order of magnitude smaller, or about 1 mrad. At 11.5 (20) cm radius from the interaction point, this corresponds to a spatial separation of about 115 (200) μm. It is clear that conventional silicon microstrip detectors (with strips a few cm long) are much less suitable in this region close to the beams than are the pixel detectors proposed here.

A pixel detector would not suffer from this ambiguity or resolution problem, even at the smallest radius. It could even solve the ambiguities in the layers of microstrips further out. Those could then be crossed at 90° in order to obtain the best resolution in both **z** and **r-ϕ**. (We have taken all the silicon micro-strip planes to have 50 μm strip pitch in ϕ and 200 μm pitch in **z**).

(2.3) Impact Parameter Resolution.

We have estimated the 3D-impact parameter of B mesons to be roughly 260 μm, in good agreement with ref (1). The estimated 2D-impact parameter resolution of 155 μm is of course not sensitive to the **z** resolution.

Multiple scattering will induce an uncertainty of the order of

$$\sigma_b^2 \approx r_1^2 \left(\frac{0.015}{p\beta}\right)^2 t$$

at a radius r_1 (in m) for a particle of momentum **p** (in GeV/c) traversing **t** radiation lengths. For instance, a 1.8 mm thick Beryllium beam pipe represents $5\ 10^{-3}$ (radiation lengths) when traversed at 90°. For a beam pipe of radius 5cm, the resultant resolution may be pârameterised as $53/\mathbf{p}/\sin(\theta)$ μm GeV. This is quite small for particles with a momentum larger than 10 GeV/c.

Fig (2) shows the total material traversed as a function of pseudo-rapidity. We have considered each surface equivalent to 1000 μm of silicon (including detector (600 μm for pixel), readout electronics, detector overlap and mechanical structure for both support and cooling). This is probably an overestimate for silicon, since

anticipating technical advances during the next few years, one might expect the thickness of strip and pixel detectors to be reduced to 200 μm, and that of readout electronics to perhaps 150 μm. One clearly sees that, at large η, the amount of material is greatly reduced by the cone structure in comparison with a simple cylinder structure. This is because the cones are oriented more perpendicularly with respect to the tracks than cylinders.

The resolution of strips of dimension **d** crossed at an angle θ is given by:

$$\sigma_z = \frac{d}{\sqrt{12}} \sqrt{\left(\frac{1}{tg^2\theta}\right) + \left(\frac{1}{\sin^2\theta}\right)} \approx \frac{d}{\theta\sqrt{6}}$$

at small θ. Clearly the smaller the angle and the worse the resolution. The impact parameter resolution is even worse because of the lever arm between the planes and the vertex position.

These resolutions are manifested in the impact parameter resolution. This has been calculated in three and two dimensions (neglecting the less well-measured **z** coordinate). Table (3.a) shows the obtained resolution for different pion energy for pixel of 50 x 200 μm size. Table (3.b) shows the same resolutions with an extra 15 μm alignment resolution for the plaquettes. Finally table (3.c) shows the expected resolutions for different pixel sizes.

Pion energy (GeV)	1.	5.	10.	50.	100.	1000.
σ(3D-b)(μm)	441.	105.	73.2	52.3	51.7	49.8
σ(2D-b)(μm)	273.	55.0	30.4	15.7	14.7	14.3

Table (3.a) Two and Three Dimensional Impact Parameter Resolutions for Different Pion Energy in the Detector.

Notice that the impact parameter resolution possible without the two inner pixel planes is σ(3D-b) = 143. μm and σ(2D-b) = 49.6 μm for **10 GeV pions**. One clearly sees the importance of an efficient detector with good resolution at the smallest radius.

Pion energy (GeV)	1.	5.	10.	50.	100.	1000.
σ(3D-b)(μm)	443.	107.	75.0	56.6	56.0	55.8
σ(2D-b)(μm)	274.	59.0	34.8	21.3	21.2	20.6

Table (3.b) Two and Three Dimensional Impact Parameter Resolutions for Different Pion Energy in the Detector and 15 μm alignment uncertainty

	Pixel Geometry		(10 GeV $\pi^{\pm}$)	
Segment	50 x 200	75 x 250	75 x 275	90 x 290
σ(3D-b)(μm)	75.0	86.3	89.2	92.1
σ(2D-b)(μm)	34.8	39.5	39.5	39.8

Table (3.c) Two and Three Dimensional Impact Parameter Resolutions for Four Different Pixel Geometries in the Inner Cylindrical and Conic Planes, for Pixel Planes with 15 μm alignment uncertainty for 10 GeV pions.

(2.4) Momentum Resolution

We expect the inner detector of fig (1) to be part of a mixed system containing repetitive lower resolution detectors at larger distance from the interaction point. Within the EAGLE proto-collaboration {ref (8)}, "external" tracking schemes containing scintillating fibre arrays, gas microstrip detectors and straw tubes (also imbedded in polypropylene to act as detectors for transition radiation) are being considered.

Using the momentum resolution estimation technique of ref (4), we may write;

$$\frac{\sigma_{p_T}}{p_T^2} = \frac{2}{0.3B}\sqrt{\frac{\sum^{m}_{i=1} r_i^2/\sigma_i^2}{\sum^{m}_{i=1} r_i^2/\sigma_i^2 \sum^{m}_{i=1} r_i^4/\sigma_i^2 - \left(\sum^{m}_{i=1} r_i^3/\sigma_i^2\right)^2}}$$

where $\mathbf{P_T}$ is the transverse momentum (GeV), **B** is the magnetic field (Tesla) and σ_i is the position resolution (metres) of the ith detector element at a radius $\mathbf{r_i}$ (metres) from the interaction point.

An exact figure for the eventual momentum resolution depends on the ultimate external tracking geometry decided upon, but it is possible to make some estimates in analogy with those made in ref (4). With 50 x 200 μm pixels in the inner detectors, and 50 μm (ϕ) and 200 μm (**z**) strips in the outer planes, each measurement, in the inner tracker should have an accuracy of about 15 μm in the bending (**r-ϕ**) plane. Figure (3) shows the momentum resolution at a P_T of 1 TeV of the inner tracking detector as a function of pseudo-rapidity, and the improvement possible when it is combined with tracking information from a detector with a spatial resolution of 100 μm at 1 metre radius.

(3) Mechanical Design

(3.1) Mechanical Structure

We propose to construct the detector of fig (1) from cylindrical and truncated conical detector segments. For tracking and vertex finding redundancy, each such segment will be made up from a pair of "concentric" nested arrays of either double - sided silicon microstrips or from a pair of silicon or gallium arsenide pixel detectors.

The outer two cylindrical detector segments will be fabricated of tiles or "plaquettes" of 300 μm thick, double-sided, silicon microstrip detectors. The inner cylinder will be fabricated of 300 μm thick silicon or gallium arsenide pixel detector plaquettes, backed up and bump-bonded onto an electronic readout array of similar thickness and radiation hardness. Anticipating technical

advances during the next few years, one might expect the thickness of strip and pixel detectors to be reduced to 200 μm, and that of readout electronics to perhaps 150 μm.

The outer conical end surface will be a similarly tesselated array of double sided silicon microstrip plaquettes, while the inner end surface might be silicon or gallium arsenide pixel plaquettes. We are developing a conceptual design for the support and cooling of the detector readout electronics, discussed in § 3.2.

We assume that the structures of the tracking and vertex detectors - the cylinders and the two conical sections - will be physically independent from one another. We further assume that there will be overlap between the detector "plaquettes" in both azimuth and z (co-ordinate along the beam direction). Fig (4) is a general isometric view of the complete detector, showing the nested cylindrical and conical segments. Fig (5) is an isometric view of part of the cylindrical detector, showing radial, axial and azimuthal overlaps.

It is worth noting at this point that plaquettes made up of pixels and silicon strips exhibit certain differences from one another;

(i) for the cylinders, pixel plaquettes can always be of rectangular shape, and require very little z or azimuthal overlap with their neighbours, since their readout electronics is located within the same effective sensitive area;

(ii) double sided silicon strip plaquettes with orthogonal strips and readout require readout electronics about 10 mm wide aligned along orthogonal edges on either side of the plaquette. This electronics reduces the effective surface area, so that larger z and azimuthal overlaps are required to recover the sensitive area;

(iii) double sided silicon strip plaquettes with non-orthogonal (i.e. stereo angle) strips must be diced into the parallelogram shape or it will be necessary to attach readout electronics along three of the four edges. This electronics further reduces the effective surface area, so that larger overlaps are required.

In each segment (one cylindrical, two conic), regularly-spaced support rods link two machined beryllium end plates, together with which they form the major structural supports of the segment. The channels contain indentations to locate the two concentric layers of detector plaquettes and maintain their overlaps with their neighbours. The support rods of the three

"concentric" cylindrical or conic segments are offset in azimuth to each other to avoid creating zones at constant azimuth with high multiple scattering.

(3.2) Power Requirements and Cooling

We are considering the possibility of forced gas cooling the entire structure (with air or helium) as has already been suggested by the INP Krakow group {ref (10)}. Should it not prove practicable to cool the detector with gas flow alone, we will consider a hybrid system combining gas flow with liquid cooling through hollow cooling channels in the beryllium end structures.

In the event that this proves ineffective in cooling the detector, we are considering two other back-up solutions:

(i) extending water circulation through the axial beryllium channels that support the palquettes;

(ii) cooling by the evaporation of an inert liquid (probably a fluoro-carbon) from the heat-producing electronics **{§(3.3)}**.

Table (4) shows the power requirements of the proposed detector geometry, together with the numbers of plaquettes and readout channels in each segment. Nominal power requirements of 0.4 W cm^{-2} for pixel detectors and 1.5 10^{-3} W/ch for Microstrips are assumed.

In the scheme of fig (4), we have chosen the number of cooling/support channels for the inner, central and outer cylindrical detector arrays to be 18, 30 and 48 {at radii 11.5 cm (double layer), 20 cm (single layer) and 32 cm (double layer)}. All arrays have an effective length of 100 cm as shown in fig (1). We would expect heat loads of 7.0, 1.15 and 3.72 kW respectively.

Surface with area (cm^2)	Radius (cm)	Total Surf Area (cm^2)	# Pixel/Strip Readout Channels (20% Overlap)	Power Reqd (kW)
Inner Pix Cylinder Plane 1	11.5	8686 (7226 no overlap)	$8.7\ 10^3$ r/o channels ($8.7\ 10^3$ chips of 10^4 pixels)	3.5*
Inner Pix Cylinder Plane 2	11.5	8686 (7226 no overlap)	$8.7\ 10^3$ r/o channels ($8.7\ 10^3$ chips of 10^4 pixels)	3.5*
Central µstrip cylinder	20	15297 (12748 no overlap)	$612\ 10^3$ (50µm,r-φ) $153\ 10^3$ (200µm,z)	0.92# 0.23#
Outer µstrip cylinder Plane 1	32	24134 (20111 no overlap)	$964\ 10^3$ (50µm,r-φ) $241\ 10^3$ (200µm,z)	1.50# 0.36#
Outer µstrip cylinder Plane 2	32	24134 (20111 no overlap)	$964\ 10^3$ (50µm,r-φ) $241\ 10^3$ (200µm,z)	1.50# 0.36#
Inner Pix Cone	15/23	1657 (1381 no overlap)	$1.6\ 10^3$ r/o channels ($1.6\ 10^3$ chips of 10^4 pixels)	0.66*
Outer µstrip Cone Plane 1	20/37	6718 (5598 no overlap)	$269\ 10^3$ (50µm) $87.5\ 10^3$ (200µm,z)	0.41# 0.13#
Outer µstrip Cone Plane 2	20/37	6718 (5598 no overlap)	$269\ 10^3$ (50µm) $87.5\ 10^3$ (200µm,z)	0.41# 0.13#
Total		111123 (92576 no overlap)	$20.7\ 10^3$ pixel r/o chips $4.6\ 10^6$ µstrips	15.4

Total Power Consumption 15.4 kW.

** Power requirement for Pixel detectors assumed to be 0.4 W cm^{-2}*

 # Power requirement for Microstrips assumed to be 1.5 10^{-3}W/ch

Table (4) Power Requirements of the Proposed Detector Geometry, Together with the Numbers of Plaquettes and Readout Channels in Each Segment.

For the 100 cm linear arrays of pixels from which the two innermost cylindrical surfaces {fig (4)} will be constructed, a nominal heat load of 0.4 Watt/cm^2 is assumed, almost all due to the power requirements of the readout electronics. This is equivalent to 40 μW / pixel, for pixels 50 μm by 200 μm and gives a total power requirement per linear array of 190 Watts. We are developing a support and cooling scheme in which one edge of each pair of linear pixel arrays is assumed to be in thermal contact with a (beryllium) support and cooling channel joining the detector end rings, which themselves my also be cooled, and plan to make a series of finite element analyses of different cooling geometries.

In one early simulation, a channel with 0.5 mm thick walls and an internal aperture of 7 mm (azimuthal) X 3 mm (radial) cross section has a laminar water flow of 35 cm/sec (17 cm^{-3} s^{-1}) {Specific heat of water is 4183 J/kg.°K in the temperature and pressure range 0-100°C; 1-5 bar}. Assuming perfect thermal contact, this flow is sufficient to cool the electronics so that a maximum temperature gradient of 6° C arises (azimuthally) across the pixel array.

With this mode of water cooling, we would expect to require a number of cooling channels proportional to the area of the particular surface. Since these would result in some extra material shadowing of successive surfaces of the detector, we will also study cooling by forced air or helium flow through thin drilled tubes and "hybrid" systems of cold channeled liquid and cold gas flow.

We are currently studying possible attachment schemes for the detector arrays. At their points of closest approach to the beam axis, the strip or pixel detectors could be supported from and thermally connected to the **inner** edges of the gas or liquid-carrying cooling channels so that tracking information may be obtained as close as possible to the interaction region, with the minimum amount of intervening material. At their points of furthest distance from the beam axis however, they are supported from and thermally connected to the **outer** edges of the cooling channels, giving some overlap with the inner edge of their nearest neighbouring plaquettes so that tracking information may be also obtained on both sides of each cooling channel; such information might be useful for the correction of multiple scattering errors.

Since most of the heat in the detector arrays (with the exception of that due to initial leakage current and leakage current enhancement with possible radiation damage) will be generated in

the readout electronics, we plan to more tightly thermally couple the readout electronics to the cooling channels. In the case of the silicon strip detectors, we are considering mounting the readout electronics perpendicular to the detector surface ie: radially at the location of each cooling channel: this might also help minimize the multiple scattering from silicon.

(3.3) Investigation of an Evaporative Cooling Technique.

Another method for cooling the electronics of the detector is to **(literally)** boil a liquid on it. While there is liquid in contact with the outside of the electronic chips, their maximum temperature cannot exceed the boiling point of the liquid.

The practical problem is that of continuously keeping a liquid film in contact with the electronics to be cooled, perhaps entrained in a low density, porous, thermally conductive foam.

Numerous refrigerants exist that could be used for this purpose. In this report, we consider just one, FLUTEC PP50 (Chemical Composition C_5F_{12}), manufactured by Rhone-Poulenc Chemicals {ref (11)}, with a boiling point of about 30°C. This material is non-flammable, non-toxic and environmentally stable (containing no chlorine). It has furthermore been used in the radiators of Ring Imaging Cerenkov Detectors, for which handling procedures have been developed.

At present there are no data on the radiation hardness of this or similar fluorocarbon materials or their decomposition products when irradiated. A program of radiation studies on this and other potentially interesting coolants is needed.

In one possible scheme, a series of channels (which are also part of the support structure of the detector) might be pierced with many small holes, through which C_5F_{12} is delivered in liquid or condensing vapor phase. Alternatively perhaps, if C_5F_{12} vapor is pumped into the cooling channels, the temperature drop from Joule-Kelvin expansion cooling might be sufficient to produce an atomised spray onto the electronics to be cooled. In either scheme, the C_5F_{12} will constantly evaporate from the electronics, to be picked up in a high carrier flow (perhaps several m^3/sec) of air or helium. We plan to investigate this mode of cooling.

It is possible that the concentration of C_5F_{12} in the exhaust air will be quite small, giving a non-asphyxiant cooling gas mixture. The C_5F_{12}/air exhaust gas might be passed through a drier (probably silica gel and 4Å molecular sieve), before entering a

Dewar at a low enough temperature to recondense and trap the C_5F_{12} at low vapour pressure while allowing the dry air to escape. The liquified C_5F_{12} may then be re-evaporated for delivery to the cooling channels or pumped in liquid form. A large flow of compressed air might be continually passed over the detector, providing some degree of cooling as well as acting as a carrier for the evapourated C_5F_{12}. A recirculator of this type would have many features in common with the C_5F_{12} recirculators in use at the DELPHI RICH and SLD CRID detectors.

Table (5) Shows the vapour pressure of C_5F_{12} as a function of temperature in °C. Also shown is the maximum non-condensing concentration of C_5F_{12} in the carrier gas exhaust stream. Fig (6) is a plot of vapour pressure versus temperature

Temp. (°C)	Vap. Pres. (Torr)	% Conc (Pt. Pres)	Temp. (°C)	Vap. Pres. (Torr)	% Conc (Pt. Pres)
-100	1.18	0.16	0	222.52	29.3
-80	4.18	0.55	20	502.70	66.1
-60	12.90	1.7	30	760	100
-40	36.23	4.8	40	1072.77	"
-20	92.94	12.2			

Table (5) Vapour Pressure (Torr) and C_5F_{12} Partial Pressure (% at 1 bar) vs Temperature (°C)

To find the amount of C_5F_{12} necessary to evaporatively cool the tracking/vertex detector, it is necessary to fit the vapour pressure curve to the Clausius-Clapeyron equation:

$$P(T) = P(T_{\{0\}}) \exp [- \Delta H/R \ (1/T - 1/T_{\{0\}})]$$

to find the molar heat of vaporisation: ΔH **(J/kg/mole)**.

where **P(T)**is the vapour pressure at absolute temperature **T (Kelvin)**, $P(T_{\{0\}})$ is the vapour pressure at a given absolute temperature $T_{\{0\}}$ and **R** is the molar gas constant **(8.3144 J/K/mole)**. Fig (7) shows a Clausius-Clapeyron fit to the C_5F_{12} vapour pressure curve. The gradient represents the $\Delta H/R$ ratio.

The latent heat of vaporisation **L** (in **J/mole**) can be obtained from vapour pressure data using an equation of state relation as shown

below. In a reversible transition from liquid phase to gas phase, there is a change in entropy $\Delta S = S(g) - S(l)$, such that the Latent heat of vaporisation **L** is defined by:

$$L = T\{S(g) - S(l)\}$$

One may relate **L** to changes of pressure and volume in another form:

$$dP/dT = L / \{T(V(g) - V(l))\}$$

where **dP/dT** is the change of vapour pressure over a small temperature range including the boiling temperature.

Using an equation of state (for example here the simplest: that of an ideal gas {**PV = RT**}, equation may be rewritten to yield **L (J/mole):**

$$L = \{dP/dT\}\ RT^2/P$$

Taking vapor pressure data at 20 and 40°C (boiling temperaure about 30°C), a value for the molar latent heat of vaporisation of 28.7 KJ/mole is obtained, indicating that a total flow of 0.45 moles per second or 146 g/sec (C_5F_{12} molar weight is 0.272 Kg) of C_5F_{12} liquid will be needed to keep a detector with a heat load of 15.4 KW at the C_5F_{12} boiling temperature of 30°C.

Taking the density of liquid C_5F_{12} as 1.6 Kg/litre, and the liquid-gas density difference as 137, we estimate a 15.4 KW detector will produce about 12.4 litres/sec of C_5F_{12} gas in an evaporation only (effectively ≤1°C temp rise) cooling system. This would require a 15.4 KW refrigerator to recondense the C_5F_{12}: probably using a liquid nitrogen heat exchanger as at SLD. We will continue to study these and other hybrid (liquid/gas) cooling systems.

(3.4) Power Distribution

The very large cooling requirement (15.4 kW for the three cylindrical segments alone) raises a considerable problem in power distribution. A current of 3080 A would be required if all the power were distributed at 5 Volts. We are considering the use of the cooling channels also as (symmetric) power distribution lines. We envisage power being brought into both ends of the detector

through a number of symmetrically positioned cables, which might also contain the coolant supply hoses.

We are considering using alternate cooling channels to supply +5 V and provide ground returns. Power or ground would be picked off the channels along their lengths for every plaquette position. Such cooling channels might be made from rectangular section beryllium, with a wall thickness sufficient to deliver the required 190 Watts for each pair of longitudinal double arrays of pixel detector plaquettes with very low voltage drop. As an illustration of the low impedance needed, a cooling channel DC resistance of 0.01 Ohm will cause a voltage drop of 0.38 Volts for 5 V distribution. Bringing the power onto the cooling channel from both ends will halve this loss however, but plaquettes along the length of the cooling channel would experience a voltage variation of about 170 mV, without their own (bulky) voltage regulators, themselves a significant source of extra heat.

One problem with using alternating cooling channels for the supply of different voltages is that half of them must be electrically insulated from the machined beryllium end-plates. While there is little problem in principle with the solid insulation, the insulating bushes that separate the channels from the end plates are required to be high-precision machined elements, and the cooling fluid is required to have very low electrical conductivity. This might turn out to be a problem if we need to cool the endplates themselves.

Another alternative might be to machine each channel from a low mass composite material with good thermal conductivity but low electrical conductivity. Several different current-carrying conductors might be bonded to the insulating substrate, either along its different edges, or laminated helically (and non-inductively if possible) around it, providing this can be done to maintain sufficient mechanical precision.

It is clearly preferable that as few different power rails as possible are used in the detector. Each plaquette would require its own fusible links for each power rail used, and great care will need to be taken to ensure that fault conditions do not create asymmetric power defecits, which could cause the detector to change its alignment in the large motor forces of the 2 T magnetic field.

We are also considering delivering the power to the plaquettes at a higher voltage (and lower current) by mounting them in series/ parallel combinations. Again great care is needed to avoid

asymmetric power defecits, but series connection might be possible if the signals into and out of the plaquette readout electronics are optically-coupled.

(3.5) Thermal Stability, Alignment and Survey

These issues are clearly very closely coupled, and we require that the contribution to the overall spatial resolution from thermo-mechanical, misalignment and measurement errors be small compared to the scale of the calculated impact parameter resolution afforded by the use of pixel detectors close to the beam, {table (5)} .

The alignment system and procedures proposed for this detector would have many features in common with those of the DELPHI microvertex detector system {ref (12)}. In the DELPHI detector, quartets of 32 mm x 58 mm and 26 mm x 58 mm plaquettes were assembled (joined end to end, with longitudinal overlap) on an x - y table under a microscope to verify the parallelism of strips. The mean residual of four reference marks over 12 cm relative to a straight line was typically σ = 1.7 μm.

Rectangular ceramic substrates were then attached at both ends of each quartet of plaquettes, each having a reference cylinder attached. :

After assembly of the plaquettes on the support structure, the positions of all reference cylinders were digitised on a 3-D measuring machine and the mechanical assembly of the detector measured to an accuracy of about 10 μm or about 1 part in 10,000.

The detector uses liquid cooling of the aluminium end rings. In operation, the radial position of the detector (relative to the beam pipe) is monitored with a system of proximity capacitance probes. These probes are used to correlate changes in radial position with temperature variations, and it has been shown that a temperature variation of about 3° C in this detector causes a change in radial dimension of about 10 μm {ref 13)}.

In the orthogonal tangential direction, changes in plaquette position are monitored by an array of light spots, projected onto about 6% of the plaquettes. Laser light is split onto a bundle of optical fibers, which channel it down to an array of small prisms rigidly attached to the inside surface of the DELPHI inner tracking chamber (with respect to which movements of the silicon tracking array are very critical). A tangential position shift is manifested

as a change in the strip illuminated, which can be easily detected by the silicon tracker readout system. With this system, shifts in tangential position of 40 μm have been correlated with regular temperature variations of 12 °C.

In addition, these "on-line" techniques are followed by a traditional software alignment using tracks fully reconstructed in the DELPHI tracking chambers.

(4) Silicon Detector and Electronics Design

Standard imaging applications using pixel detectors (CCD, photodiode arrays) exist. Their speed is not critical and a slow serial readout, followed by the (on chip) signal processing of a single output chanel, is sufficient. This is inadequate for high luminosity applications.

For two years, the CPPM Marseille group has collaborated in the CERN RD19 collaboration, whose aim is to develop micropattern silicon detectors for high luminosity application at LHC.

(4.1) Pixel Detector: Monolithic versus Hybrid

Two techniques for pixel detector realisation are under consideration: fabricating the readout electronics on the detector chip (monolithic approach), or sandwiching the detector and readout chips with solder in between (hybrid technique).

The hybrid approach is more flexible, allowing for separate design and optimisation of the electronics and the detector. It avoids possible compatibility problems caused by application of different processes to the same wafer. The connection of the two parts is then a major issue. The solder bump bonding method has been successfully used by our collaboration to produce several hybrid detectors, including a detector with one thousand cells, which has been tested in a heavy ion beam.

An advantage of pixels as far as detector integration is concerned, is the possibility to have the electronics and the detector on one substrate of silicon, provided its electrical properties and implantation processes are taken care of. Monolithic detectors are elegant, present minimal material thickness, are easier to assemble and possibly cheaper, but development is still needed and a major effort is under way.

Two approaches are possible for a monolithic design: implantation of the readout electronics directly onto the high resistivity wafer - which is not straightforward, essentially because of the degradation of the subtrate resisitivity during the VLSI process - or use of dedicated substrate, namely SOI, wafers where an oxide layer separates the detecting part (substrate bulk) from the processing circuitry. This is the technology we are investigating. There exist several technologies to obtain SOI wafers and we propose the use of SIMOX and ZMR processes, in collaboration with IMEC, Leuven, Belgium. Diodes implanted on SOI wafers, from which the top silicon and oxide layers had been removed, have been tested and encouraging results have been obtained {ref (14)}. A new run has been started with a whole set of test structures and electronic sub-systems.

(4.2) Prototype Design

(4.2.1) Electronics.

Starting from the LAA project design of a Direct Readout Device (DRO), we have developed several basic cells, integrated into various matrices for evaluation.

The first iteration is a RAM-like device, with line and column addressing, to read if a pixel was hit or not. Of course, this technique slowed down the system, but allowed us to test a full and quite sophisticated signal processing chain integrated within the area of each detecting element {ref (15)}. It contains a preamplifier with some shaping, a synchronous comparator and discriminator and a digital memory element.

The next generation has been developed for collider applications and uses an asynchronous comparator. Several variations were made starting from this cell. A fixed target version, with trigger capability (reset, delay for trigger decision,...) has been integrated as a 64 lines of 16 pixels matrix (so-called Omega chip), read out sequentially into a two-byte buffer, then transferred to on-board memory.

One version concentrates on the analog readout scheme, with in-cell processing including a peak detector and an analog storage element. On the other hand, being much concerned with readout speed, a group of RD19 at College de France, has developed a sparse data scan (SDS) readout that allows for reading only those pixels that are hit. This chip will be tested in a beam before the end of

this year and could be used in a LEP detector (such a pixel detector is under study for the DELPHI forward tracking).

Different readout schemes are under study at CPPM (time stamping followed by selective readout, shift register delay and trigger selection,...). All these schemes include the readout of only the hit pixels. The chips with no hit are simply skipped. This greatly reduces the readout time for a high number of channels.

The pixel electronic chips include all the readout features and do not need extra multiplexing chips (as it is the case for microstrip detector). The number of pixel electronic chips is about the same than for double sided microstrips multiplexing chips. Then, apart for the bump bonding (in the case of an hybrid detector), the estimated price for a complete pixel detector is similar to that of a microstrip detector with his electronic chips. The estimated price of a silicon detector is proportional to the surface and not simply to the number of channels.

(4.2.2) Detector assembly.

As already stated, the bump bonding technique is a major concern in hybrid detectors, as is designing sub-system assemblies to be mounted onto the mechanical structure suporting the full detector. Our approach is two fold: industrial bump-bonding and conductive glue stamping. It is recognized that bump-bonding is a long existing technology, but its use was limited (partly because of the price) to dedicated applications (sensors for military and space applications, screens, computer technologies). Few manufacturers are ready for mass-production (IBM, ST-TMS, Plessey, Hughes), and some of them are restricting this process to their own needs (IBM). We have thus started an evaluation of the Plessey process, as far as detector and electronics integrity and properties are concerned. With Plessey, we have realized our first large scale (0.5 cm^2) hybrid. In parallel, we have been working on an alternative solution - limited at present to laboratory evalution of devices - and have developed a stamping method that allows deposition of tiny drops of conductive glue, as well as an alignment tool for contacting and connecting the detector to the electronics chip.

This technique was used to bond several LAA chips onto detectors for tests, and also to start a study of the detector itself by connecting a fanout pattern on a pixel detector. We are so far limited to 50 microns dots and one hundred connections to maintain reproducibility. Investigation of this process is continuing.

As far as sub-systems construction is concerned, we are starting an effort with several manufacturers, including Plessey, for the realization of hybrids by the technique of wafer-scale integration, where several (electronics) chips are bump-bonded onto a large single piece of silicon (the detector) about the size of a wafer . One of the main issue under investigation for this work, is the behaviour of buses, conveying signals and power supplies deposited onto high resistivity silicon and the feedback as seen by the input of the electronics through the diode element.

(4.3) Tests of Prototype

The so-called LAA chip has been extensively tested at CERN {ref(15)} and by Marseille. We have successfully made the first bonding of a pixel detector to this electronic, using our conductive glue technique. Some problems have been found with this first iteration, but they have been understood and solved in the next versions we developed with RD19. The version mostly studied was designed with a view to running at WA 94, and an adjustable delay and shift register-like electronics were added to enable the use of an external delayed trigger from the experiment. This chip was provided with electrical input to allow for test without a detector.

Measurements have been made of the threshold characteristics of the amplifier/comparator circuit and a charge equivalent variation of 240 e^- was measured for a transition from 2% to 98% of the response (4 σ) which coresponds to an ENC of 60e^-. The average threshold was found to be quite high, however, around 2800 e^-, with a spread of 430 e^- r.m.s.

The delay distribution was found also to be non-uniform, with a (not completly understood) left-right asymmetry. Nominal value is around 500 ns {ref (16)}.

All these measurements have been performed also at Marseille, using a Camac chain to record full map of the detector when irradiated with a β source. We have shown that the left-right asymmetry of the delay distribution was a column effect, thus probably due to current distributions from one column to the other.

Three hybrids, consisting of the chip described above, bump-bonded with detectors manufactured by Canberra, and bonded at Plessey, Caswell, were put in a beam at Omega-WA94. A display of a event with a large number of hits {fig (8)} is shown. The average hit

number is around 3.3, large enough to demonstrate the good capabilities of pattern recognition. Due to the very severe environment of the heavy ions, some properties like noise and efficiency of the hybrid are difficult to measure, but estimates have already been found by early offline analysis. Noise less than 0.01 % was found, in connection with a efficiency greater than 99.5 %.

We have worked on the track reconstruction problem, in order to check the resolution and we have measured 23.5 μm, in accordance with the predicted 22 μm.

(5) LHC Radiation Dose and Radiation Hardness

(5.1) Expected Radiation Doses at LHC

Using JETSET and PYTHIA, we have estimated the number of charged particles expected at LHC. Table (6) shows the radiation dose expected from charged particles only, at a luminosity of 2 10^{34} cm^2 sec^{-1}, at a given radius **R** and distance **D** from the interaction point.

Dose in Mrad/year Radius **R** (cm)	distance **D** from the interaction point (cm)				
	0	20	30	40	50
5	16.1	17.3	17.6	17.0	5.9
10	4.4	4.0	4.3	4.3	4.2
15	1.6	1.8	1.8	1.9	1.9
20	0.93	1.1	0.98	1.0	1.0
25	0.60	0.65	0.59	0.64	0.65
30	0.40	0.41	0.49	0.45	0.44
35	0.28	0.30	0.31	0.32	0.33
40	0.24	0.23	0.23	0.28	0.25

Table (6) Radiation Dose Expected (at L = 2 10^{34} cm^{-2} sec^{-1}), at a Radius R and Distance D from the Interaction Point.

We see from table (6), that the radiation dose is almost independent of **D** and depends only on the radius **R**. The level of 1 Mrad/year is at a distance of about 20 cm from the beam axis.

These numbers are in agreement with {ref (17)} for charged particles only. In addition to charged particles, γ mainly from π^0 decay are numerous. But only a small fraction of them will produce a positron-electron pair, leading to an increase of the radiation dose. This effect depends crucially on the exact geometry and the amount of material inserted between the primary vertex and the SITV detector. A Geant simulation has shown an increase of the order of 7 %, mainly due to low energy electrons. This effect is slightly larger in the cones (10 %) than in the barrel (5 %) due to the increased material traversed by the γ. When the magnetic field is turned on at 2 Tesla, some low energy particles will describe spirals that may hit the SITV detector many times. The increase is of the order of 30 % of hits, slightly higher in the barrel than in the cones.
The combined effect of magnetic field and of initial γ's is an increase in the radiation dose of 43 % over the SITV detector.

The neutron fluences given in ref (18), for the case of detectors enclosed within a liquid argon calorimeter, lie in the range {3 - 6 10^{13} n/cm^2 /year} at a luminosity of 2 10^{34} cm^{-2} sec^{-1}. In addition the neutron fluence coming from the interaction is found to be around 10^{13} n/cm^2 /year at maximum LHC luminosity. Those neutrons will have a much higher momentum (around 1 GeV).

(5.2) Radiation Effects

Considering the radiation environment encountered in an LHC experiment, the radiation damage expected in a semi-conductor detector can be separated in two dominant mechanisms:

(i) Displacement damage also called "bulk effects" generated by neutrons and charged particles;

(ii) Ionisation damage called "surface effects" which correspond to the generation of electron-hole pairs and trapping of charges in the oxides and at the Si/SiO_2 interfaces.

(5.3) Radiation Effects on Pixel Detectors

(5.3.1) Expected Damage

Radiation induced lattice defects give rise to unwanted energy levels in the semi-conductor gap which act as generation or recombination centers. The electrical properties of the high resistivity Si detectors are greatly altered by these bulk effects. Three main consequences are observed:

(i) An increase in the reverse bias leakage current leading to increased noise and power consumption. The increase in current density is proportional to the particle fluence with typical value for the damage constant of 7 10^{-17} A cm^{-1} for neutrons and 3 10^{-17} A cm^{-1} for charged particles.

(ii) A degradation of the collected signal due to the trapping of the generated carriers.

(iii) A change of the effective doping concentration of the n-type highly resistive silicon due to carrier removal and creation of acceptor-like defects. At a fluence of a few x10^{13} n/cm^{-2} (reached after less than a year of operation {ref (18)}), the n-type material inverts to a p-type material. The electric field in the bulk is altered, the junction contact becomes ohmic and vice versa. This can lead to severe problems of insulation between the diodes and severe degradations of the collected signal. Furthermore, after inversion the depletion voltage increases proportionally to the fluence {refs (19,20)} and can be a serious limitation for detector operation. Surface damage may enhance surface currents and lead to interpixel insulation problems.

(5.3.2) Choice of structure

Considering the radiation effects expected, pixel structures offer non negligible advantages:

(i) The increase of leakage current under neutron irradiation is proportional to the active volume of the diode. The noise increase relative to this leakage is also much less for a small surface. As an indication, table (7) shows the equivalent noise charge at two shaping times for three different leakage currents in a 300 μm thick silicon detector with 50 μm X 6 cm microstrips.

Leakage Current (μA)	ENC (15 ns shaping)	ENC (45 ns shaping)
20	1890	3270
5.0	950	1650
3.8	825	1430

Table (7) Variation of Equivalent Noise Charge with Leakage Current at Two Different Shaping Times.

For a pixel having a surface 300 times smaller, we can extrapolate an radiation induced equivalent noise charge (ENC) of 110 for 15 ns shaping and less than 200 for 45 ns shaping.

(ii) For a 300 μm thick and 50 μm x 200 μm pixel surface, the measured signal (corresponding to the passage of a minimum ionising track) to noise ratio is 25000 e^- /60 e^-, or about 400. One can therefore tolerate a degradation a factor of 20 before being at the equivalent signal to noise ratio of a silicon microstrip detector.

(iii) The pixel detector structure is very simple compared to the double-sided microstrip structure. The direct DC coupling, allowed by good initial signal to noise ratio, permits us to forget about the oxide charge buildup and the interface state problems which may occur in AC coupled microstrips. Furthermore, the pixel is one-sided. Insulation problems following the type-inversion may then be solved in an easier way.

(5.3.3) Studies undertaken at CPPM on Radiation Hard Detector

We intend to optimize the pixel detector hardness by making simulations and electrical measurements on prototypes of pixel matrices.

Simulation software (BAMBI or PISCES-II) permits the calculation of carrier concentration and electrical field distribution in the detector structure. Simulation will be used to optimise the pixel geometry, to calculate the interpixel capacitance and evaluate the degradation of the interpixel insulation and charge collection induced by the radiation damage.

In parallel, electrical measurements (bulk and surface leakage currents, capacitance-voltage, capacitance-frequency characteristics) will be undertaken on test structures before and

after irradiation to evaluate neutron and ionization damage in materials and pixel detectors.

(5.4) Radiation Effects on Electronic Componants

(5.4.1) Requirements

We need high density VLSI mixed analog/digital electronics with a very high level of radiation hardness (>50 MRad for total dose and 10^{15} neutron/cm^2), with high speed and low noise capabilities.

(5.4.2) Expected damage on elementary components

The main degradation of bipolar transistors comes from bulk damage induced by neutrons. This leads to an enhanced recombination of minority carriers making the base current increase and the transistor gain to decrease. Another effect observed under neutron irradiation is the reverse current increase due to the creation of generation centers.

Under γ - irradiation, interface states creation and charge build-up in surrounding oxides may also enhance surface recombination (and thus decrease gain) and increase leakage currents.

The JFET being a majority carrier device does not suffer from minority carrier recombination and so is inherently more radiation hard than bipolar transistors.

MOSFETs, being also majority carrier devices, do not suffer much from bulk damage but they are very sensitive to total dose effects. Unlike the JFETs, MOS transistors are controlled by the gate electrode through a thin gate oxide and are thus very sensitive to fixed oxide charge buildup and interface state creation induced by ionizing radiation. The threshold voltage shift and channel mobility degradation are the main consequences observed.

(5.4.3) Radiation hard electronics development

Different radiation hard technologies are available and have been tested by other groups: bulk-CMOS (Harris Semiconductor, UTMC...), SOS (ABB-HAFO, Hughes Aircraft...), SOI (IBM, Sandia, Thomson TMS...).

The first purpose of SOI was to reduce the active silicon volume of MOS transistors to prevent transient radiation induced photocurrents (leading to latchup and transient upset). It appears

that this technology has also many advantages for neutron and total dose hardness {ref (21)}.

Our program is to make the pixel front-end electronics in a thick SOI technology under development (DMILL) which contains 4 types of components (CMOS, PJFET and NPN) and so allows the design of high frequency, high linearity, low noise and high hardness circuits. The first objective is to evaluate the neutron and gamma hardness of the elementary components,then to design, produce and test specific analog and digital functions. The final purpose is to implement and test under radiation a complete front-end circuit.

Conclusions

We have proposed the construction of a combined silicon microstrip and pixel detector for inner tracking and vertex finding in the EAGLE detector at LHC. We believe the combination of cylindrical and conic detector layers and the use of innermost pixel layers with outer microstrip surfaces to be very powerful.

The cylinder/cone geometry reduces the amount of material (both the effective plaquette thickness and plaquette overlap) at large pseudorapidities relative to geometries in which all the detector plaquettes are parallel to the beam axis. The inclusion of outer cylindrical layers at a radius of 32 cm greatly aids in tracking, while the pixel/microstrip combination also offers the following advantages over an all-microstrip detector:

(i) Enhanced pattern recognition performance through the better resolution of pixels for track finding in the high LHC luminosity:

(ii) Pixel inner planes will also give high precision space point close to the interaction point with an improved **z** resolution (relative to that of microstrips with small stereo angle) allowing a better determination of the beam collision point, and separation of multiple events in the same bunch crossing:

(iii) Pixel detectors positioned close to the interaction point will suffer less from radiation damage than microstrips in the same environment. Their intrinsic noise and leakage current are smaller to begin with, due to the smaller pad geometry, and proportionally greater increases in these effects are tolerable than in the case of microstrips.

References

Ref (1) Track and Vertex Detection.
D. Saxon: Proceedings of ECFA Large Hadron Collider Workshop, Aachen, Germany 4-9 October 1990, Eds. G. Jarlskog & D. Rein **CERN 90-10, ECFA 90 - 133,** 3 December 1990: **Vol. 1**, pp 339-369.

Ref (2) Top Quark Physics with B Tagging at LHC.
F. Bedeschi et al Proc1990 Aachen LHC Workshop, **Vol. 3**, pp 268 - 270

Ref (3) Silicon tracking at High Luminosity.
G. Tonelli: Proc1990 Aachen LHC Workshop, **Vol. 3**, pp 285 - 290

Ref (4) Tracking at the SSC.
H. Sadrozinski et al:
Santa Cruz Institute for Particle Physics, Preprint **SCIPP** 87/100
SCIPP, University of California, Santa Cruz, Santa Cruz CA95064

Ref (5) JETSET 7.3 Event generator Program.
CERN Computer Program Library. June 1991.

Ref (6) PYTHIA 5.6 Event generator Program.
CERN Computer Program Library. September 1991.

Ref (7) Some Remarks about the Silicon Tracker for LHC.
S. Gadomski: RD20 internal report dated January 1992.

Ref (8) Transparency Copies from EAGLE Plenary Meeting January 21, 1992

Ref (9) A Direct Observation of Quark - Gluon Jet Differences at LEP.
OPAL Collaboration G. Alexander et al
CERN PPE/91-91, Physics Letters **B265 (1991) 462**

Ref (10) EAGLE internal report by K. Pakonski, Krakow (dated 24 January, 1992)

Ref (11) FLUTEC PP50 (Perfluoro-n-pentane) Data Sheet
Rhône Poulenc Chemials, ISC Division,
Avonmouth, Bristol, BS11 9HP, UK.

Ref (12) Status of the DELPHI Vertex Detector Alignment
Methods and Geometrical Position."
H. Dijkstra et al: Nucl Instr. & Meth; **A 289 (1990) 400**

Ref (13) Status and Results of the DELPHI Vertex Detector
Transparencies of talk by W. Trishuk,
European B factory Meeting, University PARIS VI & VII
December 7 & 8, 1990

Ref (14) Proceedings 1991 Elba Conference on Frontier Detectors
(May 26-31, 1991)
To be Published in Nucl Instr. & Meth

Ref (15) 10 MHz Micro power CMOS Front End for Direct Readout of Pixel detectors.
D. Campbell et al
Nucl Instr. & Meth; **A290 (1990) 149**

Ref (16) CERN Document **ECP/91-26 (1991)**

Ref (17) XXX reference dose charged particles

Ref (18) New Dose Calculations for LHC Detectors.
G. Stevenson; Proc. ECFA LHC Workshop, Aachen, 1990,
Vol. 3, pp 566 - 583.
and G. Stevenson et al DRDC P5 Add1, March 1991

Ref (19) M. Glaser, F. Lemeilleur and E. Occelli
CERN ECP 91-16

Ref (20) D.Pitzl et al.
Nucl Instr. & Meth; **A311 (1992) 98**

Ref (21) Silicon on Insulator for Ultra-Hard Applications
J. Leray et al. Proc. ECFA LHC Workshop, Aachen, 1990,
Vol. 3, pp 666-670.

Figure Captions

Fig (1) View Showing the Proposed Detector Geometry and the Pseudo-rapidity Coverage of the Cylindrical and Conic Segments.

Fig (2) Plot of Fractional Radiation Length of Silicon as a Function of Pseudo-rapidity.

Fig (3) The Momentum Resolution at a P_T of 1 TeV as a Function of Pseudo-rapidity for the Inner Tracking Detector alone and combined with a Spatial Resolution of 100 μm at 1 metre radius.

Fig (4) General Isometric View of the Detector, Showing the Nested Cylindrical and Conic Segments.

Fig (5) Isometric View of part of a Detector cylinder, showing radial, axial and azimuthal overlaps.

Fig (6) Ln (Vapour Pressure) Vs Ln (Absolute Temperature) for C_5F_{12}.

Fig (7) Clausius-Clapeyron fit to the Vapour Pressure (Nm^{-3}) for C_5F_{12}

Fig (8) A display of a event at Omega with a large number of hits in the pixel telescope. The average hit number is around 3.3,large enough to demonstrate the good capabilities of pattern recognition.

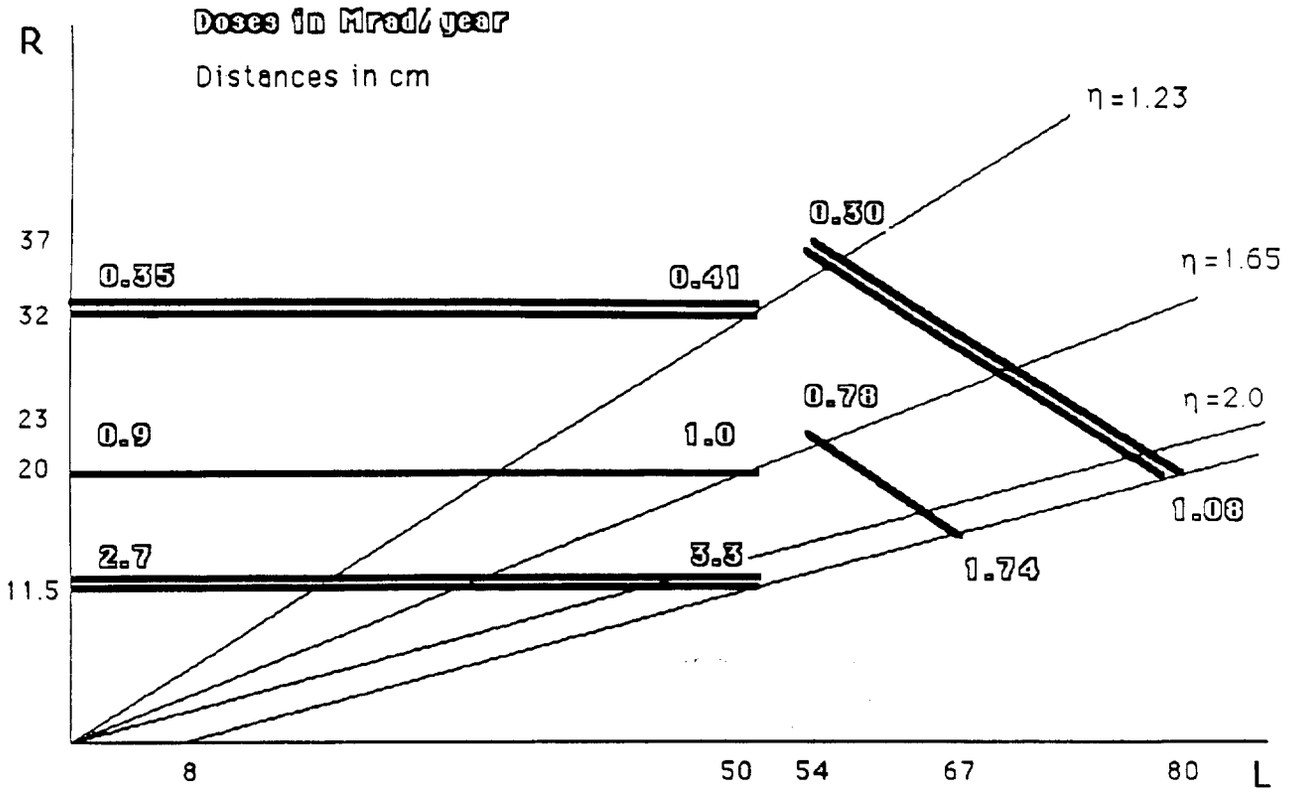
Doses in Mrad/ year
Distances in cm
R
37
32
23
20
11.5
0.35
0.41
0.9
1.0
2.7
3.3
0.30
0.78
1.08
1.74
η = 1.23
η = 1.65
η = 2.0
8
50
54
67
80
L

Fig (1)

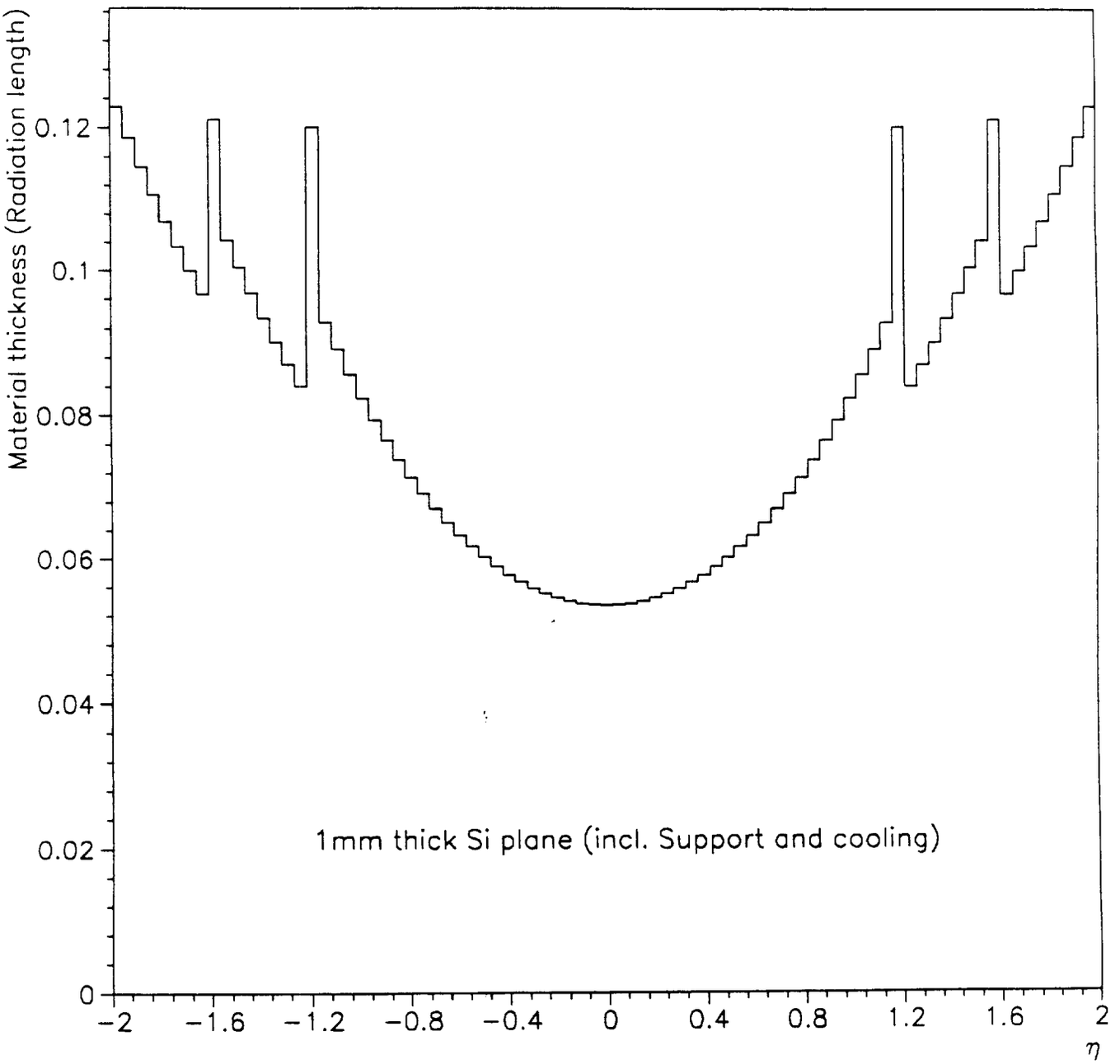
Material thickness (Radiation length)
0.12
0.1
0.08
0.06
0.04
0.02
0
−2
−1.6
−1.2
−0.8
−0.4
0
0.4
0.8
1.2
1.6
2
η
1mm thick Si plane (incl. Support and cooling)

Fig (2)

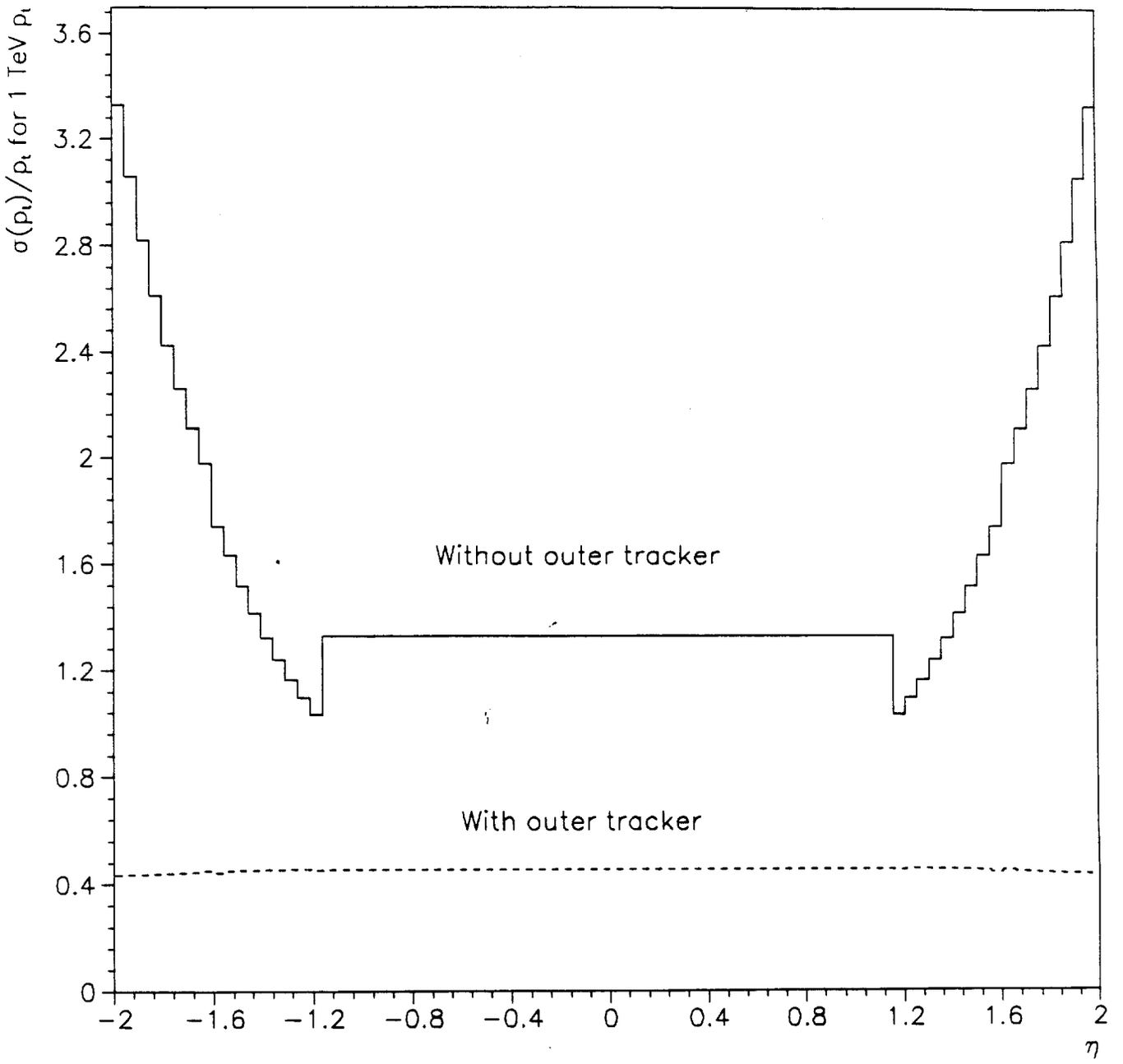
$\sigma(p_t)/p_t$ for 1 TeV p_t
3.6
3.2
2.8
2.4
2
1.6
1.2
0.8
0.4
0
Without outer tracker
With outer tracker
−2
−1.6
−1.2
−0.8
−0.4
0
0.4
0.8
1.2
1.6
2
η

Fig (3)

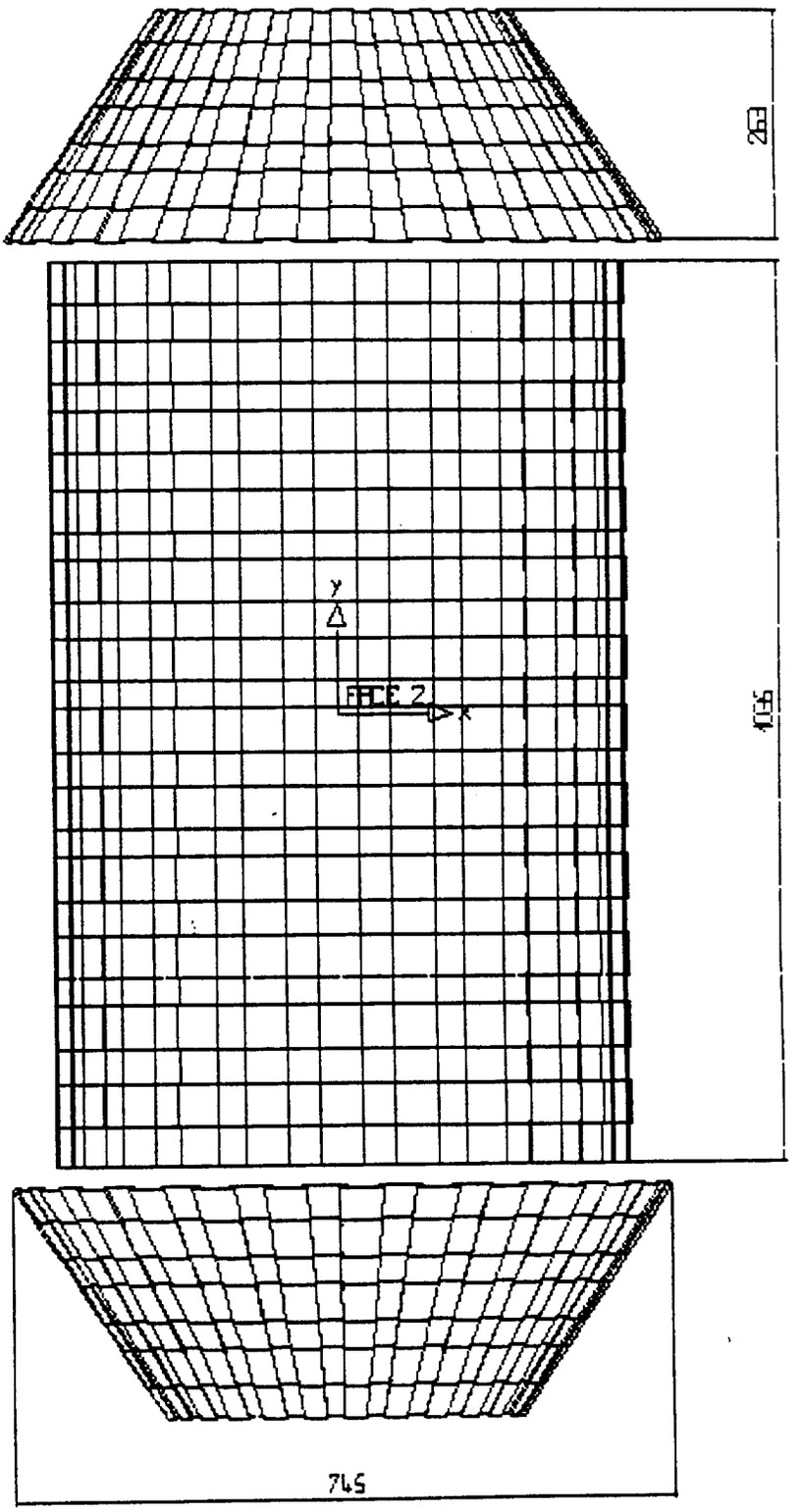

Fig (4)

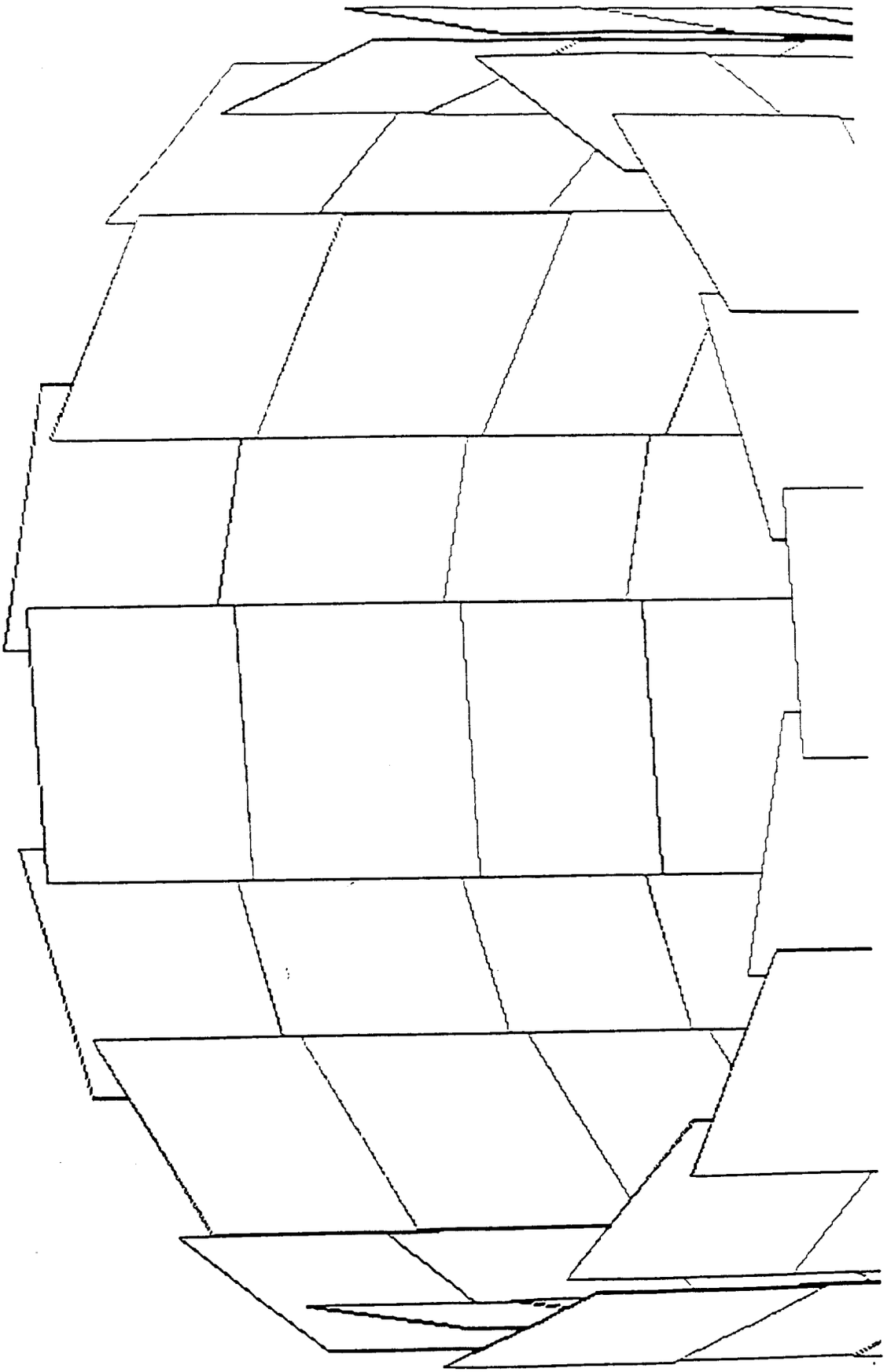

Fig (5)

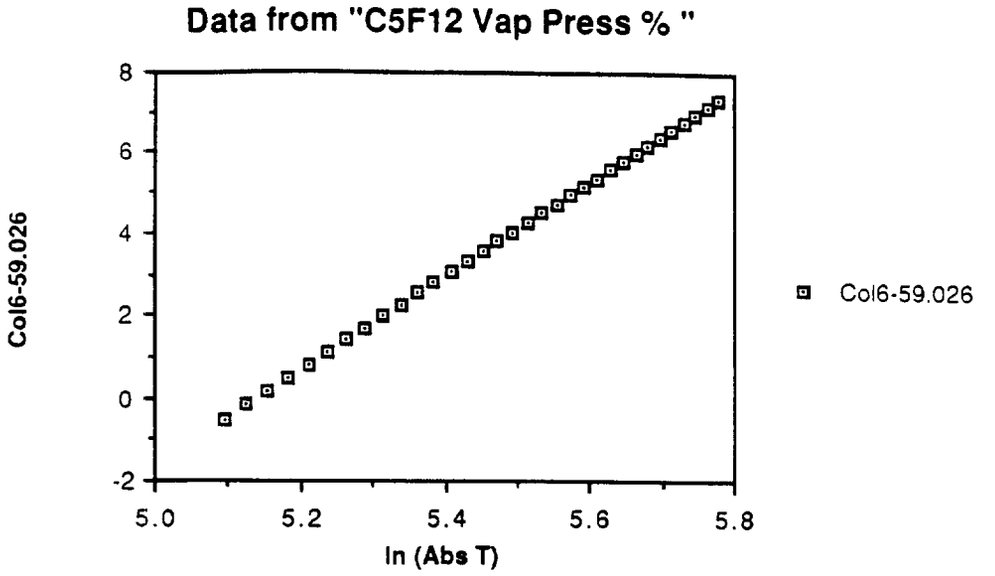

Fig (6) Ln (Vapour Pressure) Vs Ln (Absolute Temperature) for C_5F_{12}.

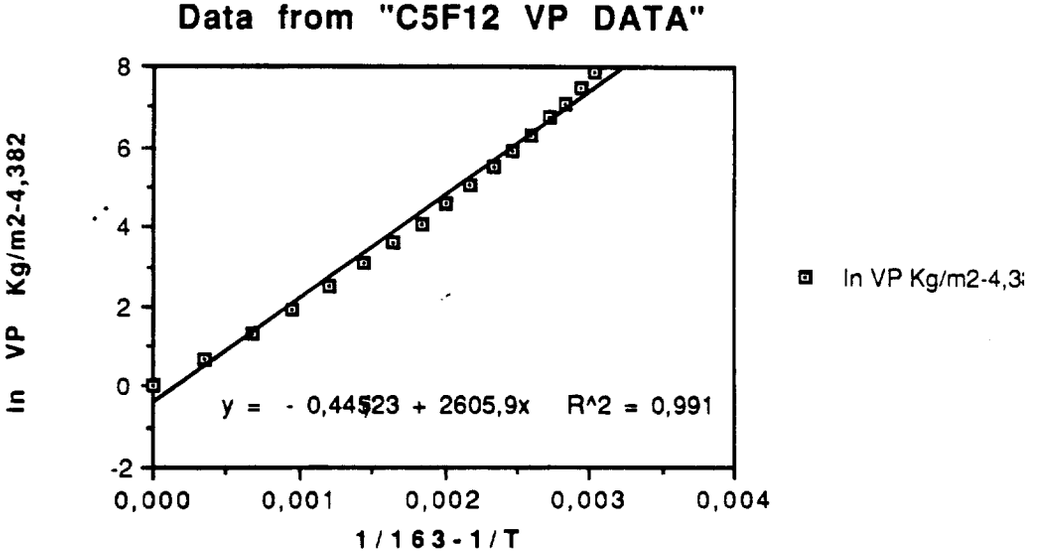

Fig (7) Clausius-Clapeyron fit to the Vapour Pressure (Nm^{-3}) for C_5F_{12}.

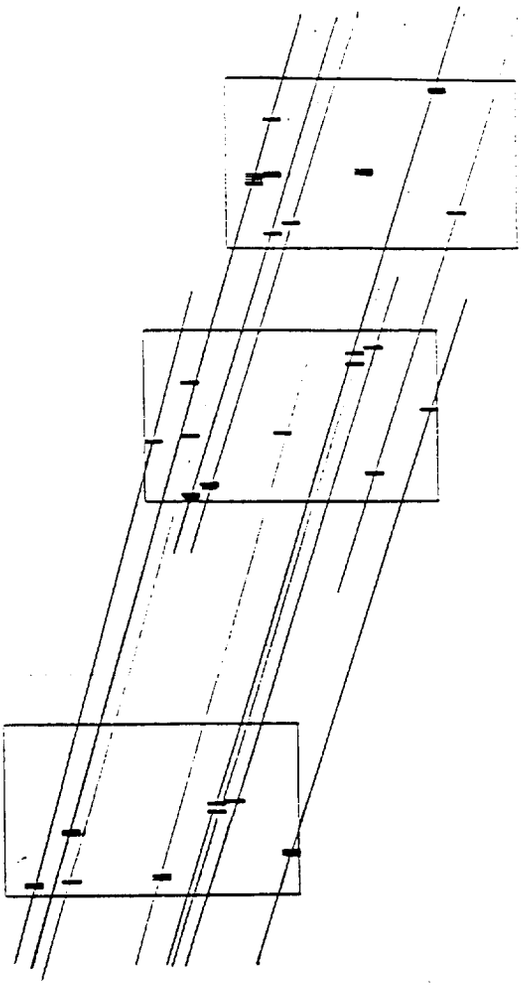

Fig (8)